CrossMark

Arecibo Radar Maps of Venus from 1988 to 2020

Bruce A. Campbell[1] and Donald B. Campbell[2]

[1] Center for Earth and Planetary Studies, Smithsonian Institution, MRC 315, P.O. Box 37012, Washington, DC 20013-7012, USA; campbellb@si.edu
[2] Cornell University, Department of Astronomy, Ithaca, NY 14853, USA; Dbc7@cornell.edu

Abstract

Over its 57 yr history, the Arecibo telescope was used to produce radar maps of Venus that pioneered our understanding of surface landforms and geologic processes. The best spatial resolution of 1–2 km achievable with the *S*-band (2380 MHz) transmitter was first used to map the surface in 1988, providing dual-circular polarization images ahead of the Magellan mission. Along with the 1988 observations, high-resolution images from observing runs in 2012, 2015, 2017, and 2020 have been archived with the NASA Planetary Data System to preserve these legacy data sets. We document the data collection and processing methods for the Arecibo Venus data, discuss unique aspects of the delay-Doppler imaging, and derive relative calibration factors linking the final multilook maps and Magellan data. The observations also allow for derivation of the circular polarization ratio and, potentially, the Stokes vector components. These results are particularly relevant for long-term monitoring of the spin rate, surface change detection, and planning for *S*-band polarimetry from the EnVision orbiter mission.

Unified Astronomy Thesaurus concepts: Venus (1763); Radar astronomy (1329)

1. Introduction

Venus science is approaching a decade-long period of renewed exploration by orbital and descent probes. From 1990 to 1994, the Magellan mission mapped about 90% of the Venus surface with a spatial resolution of ~150 m, and these data have supported Venus science for over 30 yr (Saunders et al. 1992). Missions now in development will answer the major questions raised over time about ongoing activity, the transition to a greenhouse atmosphere, and whether Venus ever had an ocean and habitable conditions. The VISAR instrument on the NASA VERITAS mission will collect *X*-band radar images and interferometry to map nearly the entire surface and topography (Smrekar et al. 2021). The VENSAR instrument on ESA's EnVision mission in the mid-2030s will bring *S*-band radar to collect high-resolution images in both senses of linear polarization (Hensley et al. 2020). The two radar data sets will be complemented by the atmospheric measurements and descent photography of the DAVINCI probe (Garvin et al. 2020).

High-resolution (1–2 km) radar mapping of Venus from the Earth began in 1988 (Campbell et al. 1989) after a series of progressively improving demonstrations and was enhanced by the Arecibo upgrades in 1997. Data from 1988 through 2020 bridge much of the time gap between Magellan and the upcoming orbiters and provide unique polarimetric information on surface properties that complements VISAR and VENSAR (e.g., Campbell et al. 1999; Carter et al. 2011). Earth-based Venus data products recently archived with the NASA Planetary Data System (PDS) include complex-valued images of the backscatter for individual coherent looks about 5 minutes in duration (Campbell 2016). These observations follow well-documented principles of the delay-Doppler method, which isolates echoes from locations on the surface by their differing range (round-trip delay) and their frequency shift due to the target planet's rotation. Second-level PDS products comprise multilook (reduced speckle, higher signal-to-noise ratio, S/N) dual-polarization maps calibrated to the thermal noise to allow for accurate calculation of the circular polarization ratio (CPR). In this work, we document the data collection and processing methods for the Arecibo Venus data, discuss unique aspects of the delay-Doppler imaging, and derive relative calibration factors linking the final multilook maps and Magellan data.

2. Delay-Doppler Radar Mapping and Calibration

Earth-based, polarimetric radar image data for Venus collected from 1988 to 2020 used the Arecibo Observatory 12.6 cm (2380 MHz) transmitter and receivers at either Arecibo or the Green Bank Telescope (GBT) in West Virginia. One sense of circular polarization is transmitted, and both senses of the reflected echo are recorded in amplitude and phase. These data have a horizontal spatial resolution of 1–2 km in the highest-resolution mode and about 8 km in a lower-resolution mode (collected in fewer observing years and not yet archived) used to increase the S/N performance for some polarimetric analyses.

The transmitted radar signal is an 8191-length pseudorandom noise (PN) code, which modulates the phase of the signal by 180° in a pattern designed to yield minimum side lobes after pulse compression (Evans 1968; Harmon 2002). The time between individual steps in the code is called the baud, and for the 1988–2020 observations, it ranges from 3.8 to 4.0 μs (Table 1). The total time length of the code, 8191 samples times the baud, is chosen to approximate the round-trip delay between the sub-Earth point on Venus and echoes from the limbs of the planet. Venus is an "overspread" target, for which the pulse repetition rate required to fully sample the span of Doppler frequencies is smaller than the round-trip time from the subradar point (SRP) to the limb. As a result, there is always a trade between aliasing of the planet's echoes in delay and Doppler shift. Many single-look images will show "folding" of the echoes in delay at high latitudes and in frequency close to the limbs.

Table 1
Observing and Mapping Parameters

Frequency	2380 MHz
Wavelength	12.6 cm
Baud	3.8–4.0 μs
Signal coding	8191-length PN
Bandwidth	263–250 kHz
Transmitter	Arecibo Observatory
Receiver	Arecibo (1988, 2015, 2017, 2020)
	GBT (2012)
Polarization	SC
	OC
Map projection	Sinusoidal equal-area
Map resolution	1 km pixel^{-1} for 6051.0 km radius
Map size	20,000 columns × 12,000 rows
Map center longitude	335°E

Figure 1. Single-look delay (vertical axis) and Doppler (horizontal axis) image of the northern hemisphere of Venus in OC polarization converted to magnitude and scaled logarithmically (in decibels). Zero Doppler shift is at the center of the image, with maximum Doppler shift from the limbs of the planet along the left and right edges. The sub-Earth point on Venus is at the top center. The region of strong quasi-specular scattering near the sub-Earth point is very bright. This is the last Arecibo image of Venus collected prior to the collapse of the telescope, from 2020 May 30.

Two observing geometries have been used for Venus observations over this period. For most observations, the Arecibo telescope (293°14′50.″3E, 18°20′39.″1N) was used for both transmission and reception (monostatic). For the 2012 observations, Arecibo was used to transmit the signal, and echoes were recorded at the GBT (280°09′36.″7E, 38°25′59.″1N). This bistatic approach was tested as a means to obtain longer potential integration periods for finer spatial resolution along the frequency axis, but the loss in isolation between hemispheres due to the wider GBT beam pattern offset any such gains.

Individual looks are limited to about 5 minutes' duration by the round-trip light time for Venus near inferior conjunction, which allows 8192 sampled echoes for each look (corresponding to a duration for each look of 8192 × 8191 times the baud listed in Table 2). The Doppler-shifted signals have a bandwidth corresponding to the limb-to-limb frequency span, sampled in frequency at the inverse of the integration period. The value of the frequency span may be obtained from ephemeris predictions, but in practice, a robust estimate is also obtained by measuring the frequency width of echoes at some value of the round-trip delay. The signals are low-pass-filtered to limit the background thermal noise component. Echoes in the same sense as that transmitted are termed same-sense circular (SC), and those in the opposite sense are termed opposite-sense circular (OC).

The echo signals are mixed to baseband and sampled in quadrature (amplitude and phase) in both senses of circular polarization using 4 (GBT) or 12 (Arecibo) bit analog-to-digital conversion. Two methods were used to compensate for the gross Doppler shift between the observing station and Venus. For the 1988 data, no compensation was applied during the observations, so an optimum change in Doppler frequency with time was derived using an autofocus technique during the correlation with the PN code. For all later data, ephemerides provided by different programs were used to impose a time-varying frequency shift to place the subradar location on Venus at zero Doppler.

The individual (single-cycle) code records are first range-compressed by correlation with the transmitted PN code. With the data set up as an array with round-trip time delay increasing down the rows, a Fourier transform of each row then yields a delay-Doppler image (Figure 1). Over the short duration of the radar looks, there is no significant change in either the delay relative to the SRP or the Doppler-frequency location of 1 km resolution cells on the surface. This means that no range migration or phase focusing is required in the processing. The single-look S/N is also low enough that no windowing (such as a Hann function) 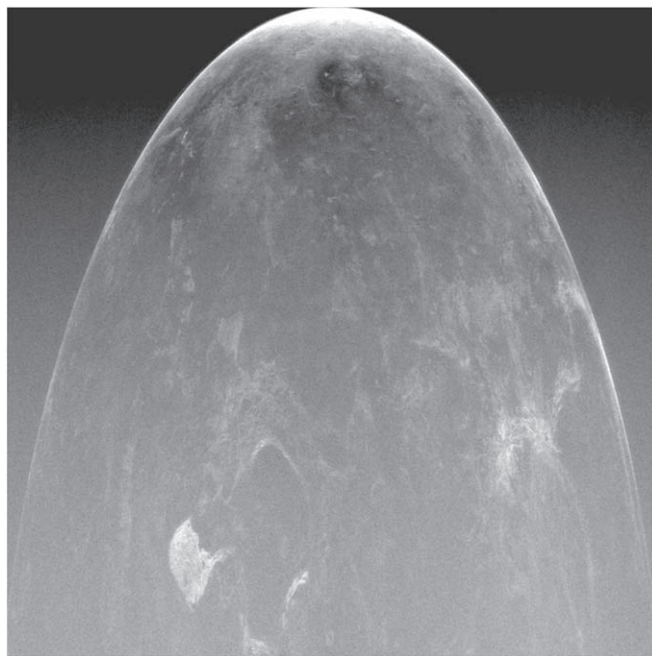is required, as any transform side lobes are below the noise threshold of the image. An important application of single-look, delay-Doppler images is the tracking of surface features over time, leading to an improved estimate of the Venus length of day (Campbell et al. 2019).

As with all delay-Doppler maps of distant objects, there is an inherent ambiguity between echoes from points in the northern and southern hemispheres of the visible face of the planet. This will fold strongly reflective features into the opposite hemisphere (Figure 2(a)), an effect mitigated by two approaches. First, the antenna is pointed about 1′ away from the SRP to the north or south of the hemisphere of interest. This places the undesired hemisphere farther from the beam center and thus at a lower transmitted power and receiving gain. Second, the image locations of echoes from the undesired hemisphere, after mapping to latitude–longitude format, shift as a function of time. Summing of multiple looks thus tends to reinforce returns from the hemisphere of interest and blur those from the ambiguous points (Figure 2(b)).

In making a map of Venus for each observing year, the goal is to increase the S/N and decrease the impact of radar speckle noise on the uncertainty of the echo values. Summing N power maps for individual looks leads to a $\sqrt{N}$ improvement in the S/N and a $1/\sqrt{N}$ reduction in the speckle. For example, adding 100 looks leads to a factor of 10 improvement in S/N and reduces the standard deviation of any radar power value from 100% of that value (at one look) to just 10% (Miller 1981). We need to map the radar data to a common projection in order to sum over multiple looks using a three-dimensional coordinate transformation to convert locations in a delay-Doppler image to latitude–longitude coordinates. Key inputs to this transformation are the location of the SRP during each look, the spin rate of Venus (i.e., the motion of the SRP), and the angle between
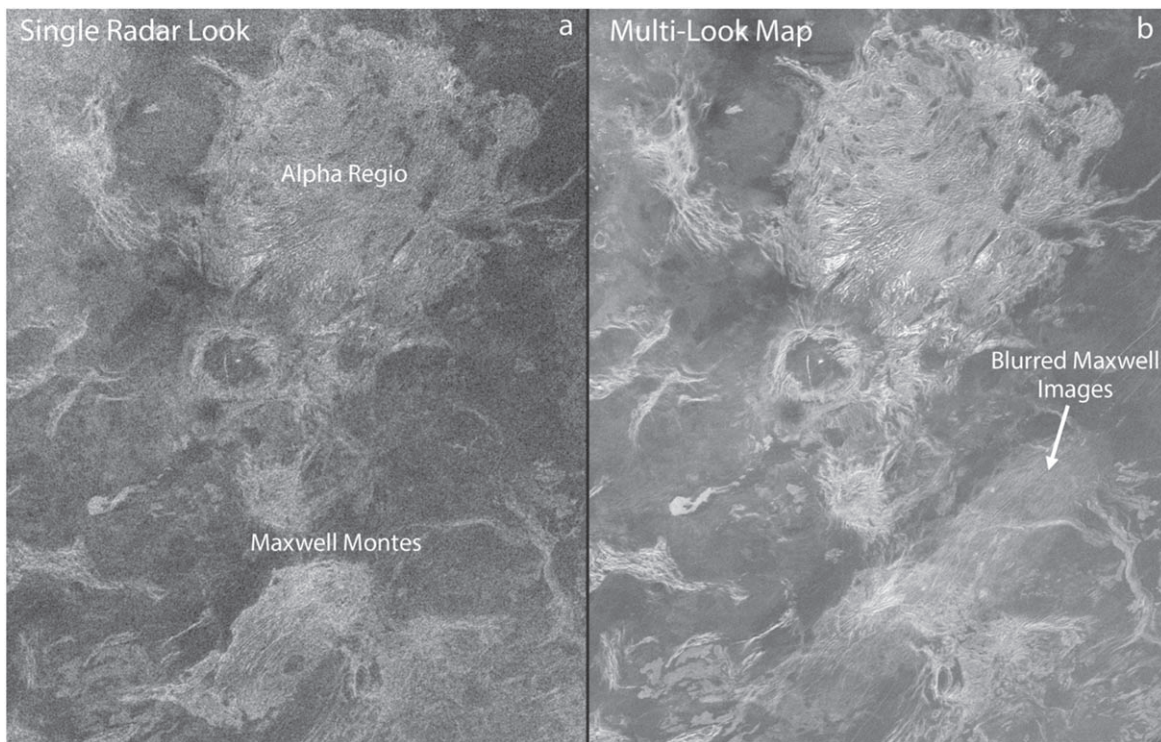
Figure 2. Radar images from 2015 of Alpha Regio and plains to the south. In panel (a), the oval bright feature south of Alpha is the sharp, folded-over image of Maxwell Montes in the northern hemisphere. In panel (b), multilook summing has blurred the series of looks in which the image of Maxwell is shifting across the region. This reduces the echo strength of such north–south folded features, but they can clearly impact geologic studies.

Table 2
SRP Locations and Number of Looks for Venus Observations

Year	Hemisphere	SRP_{LAT}	SRP_{LON}	Looks	Baud (μs)	Cal. Factor (dB)
1988	N	1.36	334.24	28	4.0	+4.4
1988	S	−1.53	322.56	29	4.0	+3.9
2012	N	−2.74	330.28	25	3.8	+3.4
2012	S	−2.68	330.62	48	3.8	+1.2
2015	N	8.16	329.75	25	3.8	+1.7
2015	S	8.02	328.87	33	3.8	−1.1
2017	N	−9.45	343.26	42	3.9	0.0
2017	S	−9.41	343.50	48	3.9	0.0
2020	N	−2.69	335.32	36	3.8	+4.8
2020	S	−2.99	333.78	48	3.8	+3.2

Note. Tabulated SRP locations reflect averages over the observations of a given hemisphere in each year and may be used to calculate approximate incidence angles for each map pixel. The SRP longitudes are corrected for the refined spin rate from Campbell et al. (2019). The baud is the time sampling of the round-trip echoes. Calibration factors are to be applied to the maps in each year to provide a relative calibration to the 2017 data for each hemisphere. There is presently no calibration connection between the 2017 maps for the northern and southern hemispheres.

the spin axis and the north–south axis. All of these may be derived from ephemerides provided by the JPL Horizons online service (http://ssd.jpl.nasa.gov/horizons.cgi). An example of one approach to the coordinate transformation is found in Campbell et al. (2007).

Calibration of the SC and OC echoes to the background thermal noise is crucial to analysis of scattering mechanisms through values such as the CPR (Campbell & Campbell 1992). Ideally, the upper left and right delay-Doppler regions of Figure 1 would be entirely "off Venus" to provide a noise reference. In practice, however, the frequency aliasing of the planet's limb regions and the modest blurring of PN code signals after pulse compression means that users must select a sample region that represents the lowest possible average echo.

A simple method is to average down the delay-Doppler array by a large factor and choose the lowest echo power value in the resulting image.

3. Multilook Maps

After single-look processing (Section 2), the calibrated and reprojected data are summed over multiple looks. This increases the S/N of the image and decreases speckle, while echoes from the ambiguous hemisphere are minimized to the degree that they move across the mapped hemisphere over the full observation period. In many cases, summed maps are further normalized by an empirical "scattering law" (which implicitly contains the atmospheric path-length attenuation
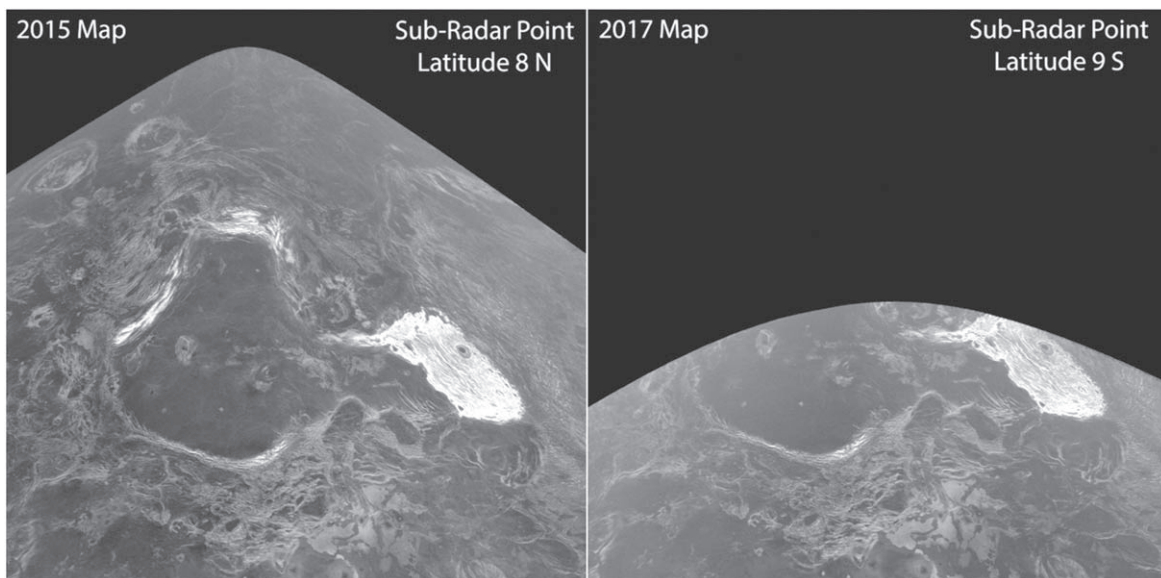
Figure 3. Comparison of coverage area on Venus with varying SRP latitude. The maximum span of the SRP latitude at conjunction is between about 8°N and 9°S. When the SRP is in the northern hemisphere in 2015 (left), more of the high northern latitudes are visible. Both images are truncated at 76° incidence angle (Figure 4).

effects with incidence angle) for the SC and OC returns that allows large-scale shifts between the SRP and limbs to be removed to emphasize subtle local backscatter variations (Muhleman 1964; Pettengill et al. 1988; Saunders et al. 1992).

A more detailed analysis of surface and subsurface scattering properties may be achieved through the Stokes vector components formed from the complex data over a number of looks (Carter et al. 2004, 2006, 2011). Because the angle between a linear-polarized signal (e.g., the H- and V-polarized components of the circular transmitted wave) and the normal to the surface rotates over time, individual looks must be corrected for this changing "parallactic angle" to ensure a consistent polarimetric coordinate frame (Carter et al. 2006). With this correction, the four Stokes vector terms may be accurately summed over a single day's looks to improve the derivation of parameters such as the degree of linear polarization. To date, the Stokes vector technique has been used primarily with data that have an 8 μs baud due to the greater S/N for each look.

The mosaicking process for the multilook data archived with the PDS warps the OC looks of any given observing year to tie points in the first look of that period. Up to 60 tie points are chosen manually for widely distributed sites with high backscatter and sharp features. This leads to reasonable fitting of surface features, but second-order polynomial warping does not yield consistent matching results across a large area. The SC looks are then warped using the same second-order coefficients, so the two images have identical geometry and can be used to form the CPR. The quality of the 2012 maps is about a factor of 2 worse in spatial resolution than other years due to unresolved phase stability issues from the receiver setup. All maps are 20,000 columns by 12,000 rows, with the lower edge of the northern hemisphere maps at 25°S and the upper edge of the southern hemisphere maps at 20°N. The map projection is sinusoidal equal-area centered on 335°E with a scale of 105.6099 pixels deg^{-1} (1 km horizontal sampling for a 6051.0 km planetary radius).

Coverage of each hemisphere differs with the latitude of SRP location (Table 2), which cycles through values of about

+8° (2015), ±3° (1988, 2012, 2020), and −9° (2017). More southerly SRP locations reveal a greater area toward the south pole (e.g., Lada Terra), while northern excursions of the SRP show features at a higher northern latitude (e.g., Maxwell Montes; Figure 3). The incidence angle at any given location changes as well, with concentric rings of equal angle centered on the SRP (Figure 4).

The multilook mosaicked images are truncated to angles <76° in order to avoid foldover of the very bright subradar region into delays greater than the time window of each pulse (8191 samples at the baud for that year in Table 2). Regions near the SRP are not mapped for incidence angles <15°, as the spatial resolution in the range direction exceeds 3 km at smaller angles. As an arbitrary limit based on the visible degree of north–south foldover, the maps are also cut off within 450 km (about 4° of latitude on Venus) of the Doppler equator.

In using the mosaics for geologic mapping or change detection, care must be taken in identifying features that may be folded over from one hemisphere to the other by their identical position in delay and Doppler space. In any single look, these folded features are sharp and often readily apparent, such as Maxwell Montes appearing in the southern hemisphere (Figure 2(a)) or Alpha Regio appearing in the north. The summing of many looks will smear these echoes and reduce their brightness (Figure 2(b)), but bright lineaments, craters, or a general "haze" may still be evident, especially on radar-dark terrain of the desired hemisphere. With a number of maps from different observing years, coverage of areas without north–south folded features in one year may be substituted for poorer data in other maps. This is especially effective for the SC maps, which have less sensitivity to incidence-angle changes.

4. Power Calibration

Each radar look is normalized to the background noise, and the mosaicked maps are averaged in power by the number of summed looks. Ideally, these "S/N" values would be comparable among all observing years, but there are changes over time in the transmitted power and the gain of the antenna(s). In particular, the 1988 data were collected prior to the upgrade of
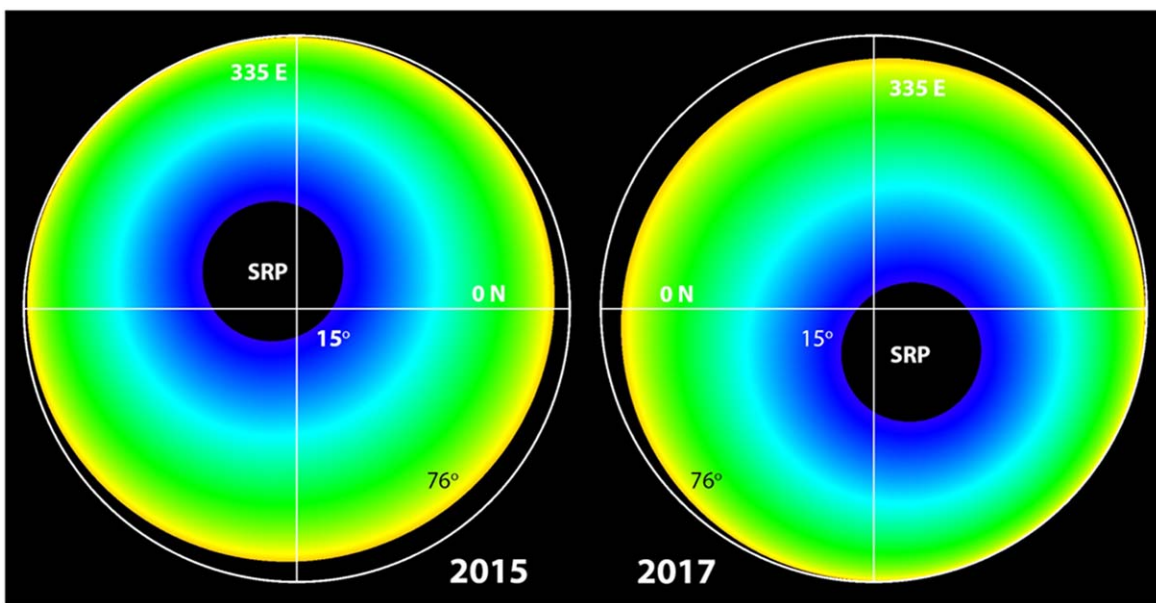
Figure 4. Radar incidence angle on the Venus surface for two observing years with different SRP locations (Table 2). The incidence-angle variations form concentric circles around the SRP. We have truncated the angle range to 15°–76°, as used for the PDS image products. Orthographic projection is centered on 0°N, 335°E.
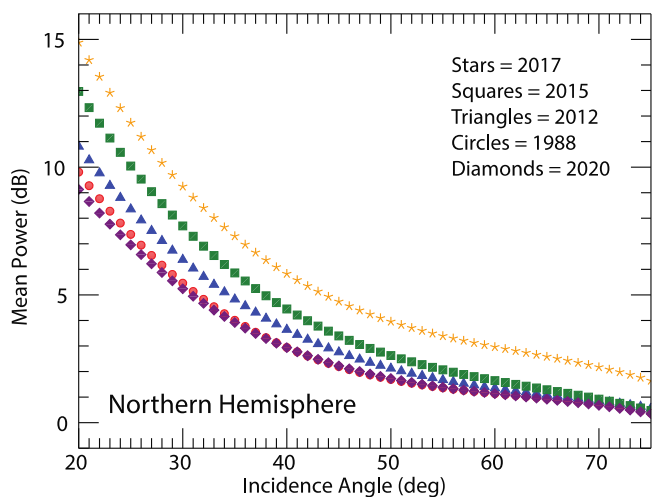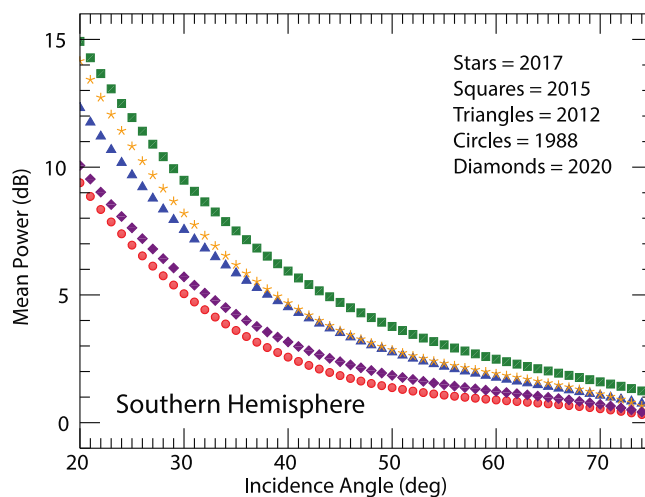

Figure 5. Plot of third-order fits to mean echo power (decibels) relative to the noise background vs. incidence angle for northern hemisphere observations from 1988, 2012, 2015, 2017, and 2020.

Figure 6. Plot of third-order fits to mean echo power (decibels) relative to the noise background vs. incidence angle for southern hemisphere observations from 1988, 2012, 2015, 2017, and 2020.

the telescope and the *S*-band transmitter, so the power level is several decibels below that in 2015 and 2017. The 2012 data were collected using Green Bank for reception, with a loss of gain due to the smaller antenna. Finally, the 2020 data were collected with only half of the possible transmitting power and the dish gain down about 2 dB due to hurricane damage.

We can derive an offset value to bring the maps into approximate relative calibration in echo power. Because the region near the SRP in every observation is on regional plains, the scattering behavior with incidence angle, ϕ, is expected to be relatively similar. We do expect a significant difference, however, in the angular scattering law between the OC and SC echoes. As was shown from early lunar radar experiments (Hagfors 1967), the OC echo is characterized by a strong quasi-specular reflection at zero incidence and a rapid drop in power out to $\phi = 10°$–20°. Beyond that point, the OC echo has a generally $\cos^{1.5}(\phi)$ behavior with ϕ. The SC return is much

weaker than the OC reflection at the SRP and declines over the entire angular range with a $\cos^{1.5}(\phi)$ dependence.

We use a third-order polynomial fit to the mean OC echo power for each year against incidence angle to capture the shape of the angular scattering law. These do show similar trends, with offsets related to the effects of transmitter power and antenna-related gains (Figures 5 and 6). Based on these offsets, calibration factors relative to the 2017 observations (for 20°–30° incidence angles) are presented in Table 2. As long as these factors are always applied to both polarizations for a given year, the CPR values are not affected and should differ between the years primarily due to incidence-angle variations.

The effects of the transmitter upgrade are apparent between 1988 and later years, with that advantage partly lost in using the GBT for 2012. The 2020 data are, as expected, also significantly lower in power than the 2017 runs and comparable to 1988 for the northern hemisphere. The northern hemisphere
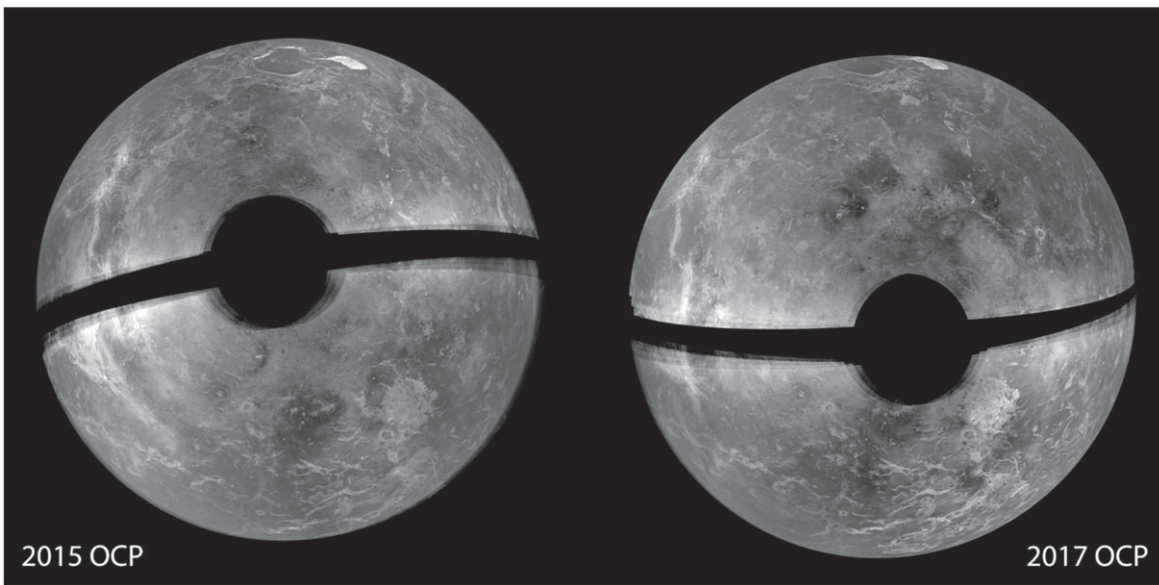
Figure 7. The OC maps of Venus from 2015 and 2017, normalized to the scatter law from Equation (1). The center of the orthographic projection is 0°N, 335°E, matching that of Figure 4. The dark horizontal band is due to the limit we placed on echoes within 450 km of the Doppler equator.
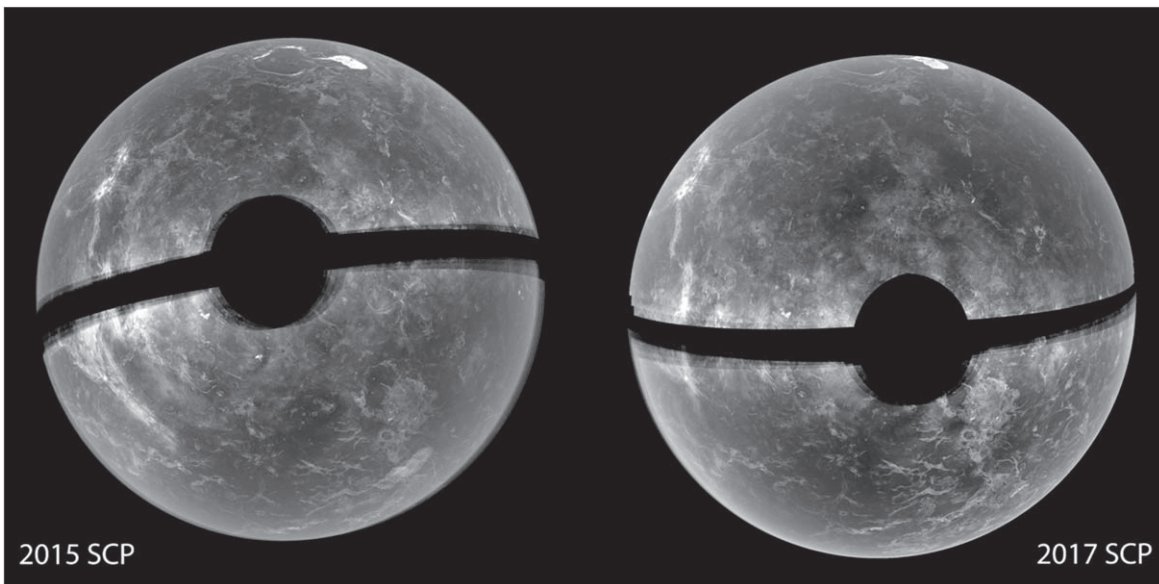

Figure 8. The SC maps of Venus from 2015 and 2017. The center of the orthographic projection is 0°N, 335°E, matching that of Figure 4. Images are normalized to $\cos(\phi)$ of the incidence angle. The dark horizontal band is due to the limit we placed on echoes within 450 km of the Doppler equator.

OC scattering function for 2017, which can be used to normalize image maps for easier comparison, is given by

$$P_{\mathrm{dB}}(\phi) = 35.34 - 1.41\phi + 0.021\phi^2 - 0.00011\phi^3, \quad (1)$$

where the values of ϕ are in degrees. We adopt a $\cos(\phi)$ form for the SC scattering law based on the earlier lunar observations and our empirical scaling tests. Normalized OC and SC multilook images for Venus in 2015 and 2017 are shown in Figures 7 and 8.

The transmitted power, antenna beam pattern, and receiver gain are not measured with accuracy, so it is not practical to derive an absolute calibration of the Arecibo echoes to the dimensionless σ_{o} backscatter coefficient. This type of calibration is achievable by comparison to swaths of the calibrated Magellan data with similar incidence angles (Campbell et al.

1999). The Magellan incidence angle, ϕ_{M}, used in the primary mapping phase decreases with latitude from $\phi_{\mathrm{M}} \sim 45°$ near periapsis around 10°N to $\sim 25°$ at the highest latitudes (Saunders et al. 1992; Campbell 1995). The incidence angle of the Earth-based data, ϕ_{A}, forms a concentric pattern away from the SRP (Figure 4). As a result, the overlap region where $|\phi_{\mathrm{M}} - \phi_{\mathrm{A}}|$ is less than some tolerance traces an arc across the Venus surface (Figure 9). That swath is different in spatial location and possibly total area between Arecibo observing years with different SRP locations.

After identifying the region of overlap for $\pm 2°$ of incidence angle, we average at the 10 km scale the echo power values in both data sets and plot the results (Figure 10). Note that each data point comes from an absolute incidence angle different from the others; we only need to have the difference between
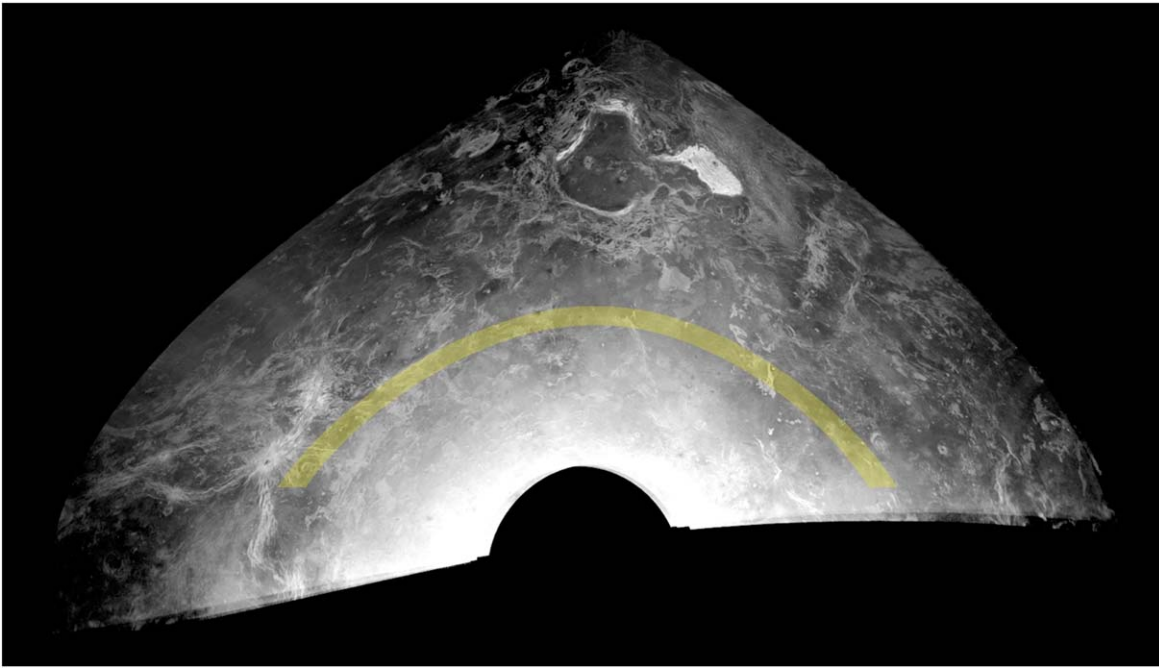
Figure 9. The overlap region of the incidence angle for the 2015 Arecibo data and Magellan Cycle 1 coverage is shown as a yellow overlay on a 2015 OC image. The tolerance for a difference in incidence angle is $\pm 2°$. The range of latitude is truncated at 20°N, such that the overall range in incidence angle within the swath is about 35°–45°.
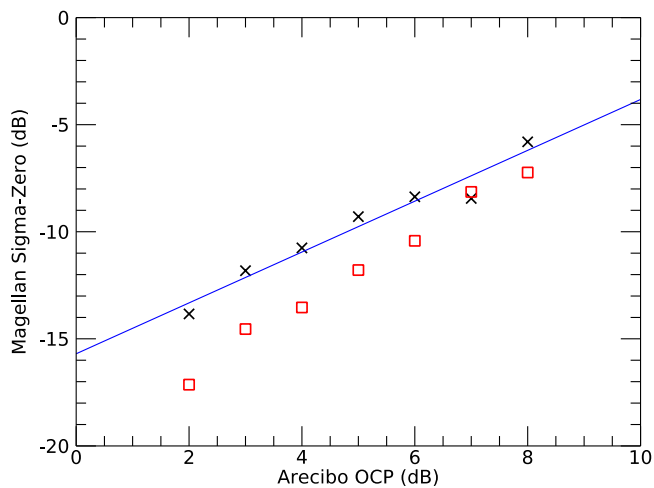

Figure 10. Plot of mean Magellan backscatter coefficient value vs. 2015 (crosses) and 2017 (squares) Arecibo OC echo for overlap regions. The blue line is best-fit linear function for the 2015 Arecibo data where the S/N is >3 dB. The slope of this line is 1.08, indicating a good agreement with the changes in Magellan backscatter. The 2017 data merge with the 2015 trend only at the highest backscatter.

the Arecibo and Magellan data be small. Our comparison of the Arecibo 2015 OC echoes and Magellan HH returns (Figure 10) shows a best-fit linear function of about

$$\sigma_o(dB) = -15.02 + 1.08 * AO_{2015}(dB) \qquad (2)$$

when the S/N of the Arecibo data is >3. The slope is close to unity, as expected for a properly calibrated signal-processing chain. For the 2017 data in this same plot, the slope of the line is significantly greater but merges with the 2015 trend at the highest surface brightness. It is likely that the Magellan overlap region with the 2017 data, which is significantly smaller than

that for 2015, may capture a biased sampling of the lower-brightness terrain (such as radar-dark crater ejecta as opposed to low-return plains). The scalar offset from Magellan echoes suggests that the 2015 Arecibo data have a noise-equivalent sigma zero of around −15 dB for the incidence-angle range of 35°–45°, represented by the overlap swath in Figure 9. This can be compared with the typically cited values of −20 to −25 dB for Magellan.

5. Radar Polarimetry from Arecibo and EnVision

The Arecibo CPR values can be related to the small-scale (2–10 cm for *S*-band echoes) surface roughness of geologic features such as lava flows, crater ejecta, impact melt outflows, and possible pyroclastic deposits (e.g., Campbell & Campbell 1992; Campbell et al. 2017). Because the dimmer SC echo limits the analysis, the higher S/Ns of the 2015 and 2017 data allow for CPR studies of areas further toward the limb of Venus visible at these times. One example is western Eistla Regio, dominated by the volcano Tepev Mons and two coronae (Didilia and Pavlova) with suspected pyroclastic runout deposits on their western margins (Figure 11; Campbell et al. 2017). These pyroclastic units have CPR values of 0.5 or greater, consistent with the properties of very rough terrestrial lava flows (Campbell 2009). Areas above a critical elevation where high-dielectric materials occur in equilibrium with the atmosphere, such as the summit of Tepev Mons and the high western and southern portions of the Pavlova annulus, have CPR values around unity.

The Earth-based dual-circular data will complement EnVision *S*-band mapping in the two senses of linear polarization (HH and HV) to better measure surface characteristics. For example, the ratio of the HV- to HH-polarized power tends to reach a maximum of ∼one-third on very rough surfaces, where the scattering behavior is like that of randomly oriented small
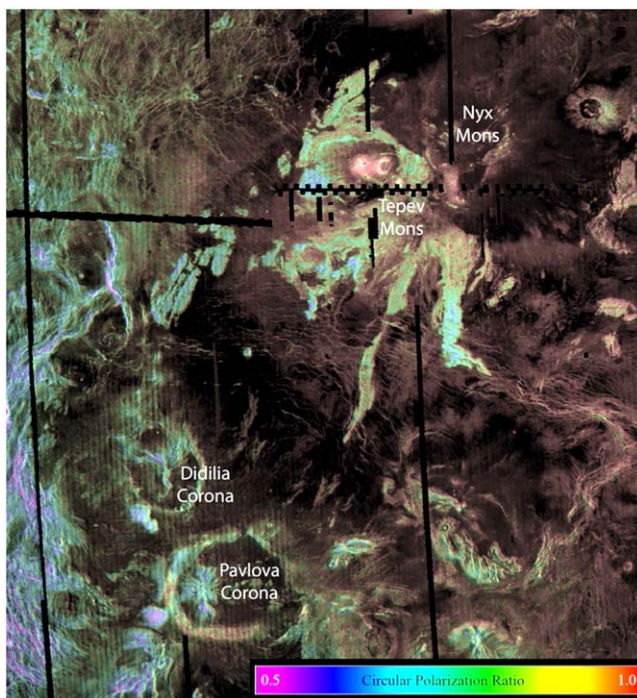
Figure 11. Arecibo 2017 CPR overlaid on the Magellan image for a portion of western Eistla Regio (10°–35°N, 32°–55°E). Very high values (red) are associated with terrain above a critical elevation of ~6054 km planetary radius. The low SC echoes from this limb region limit the detected CPR values to those above ~0.5, which correspond to very rough terrestrial volcanic surfaces.

dipoles (Campbell et al. 1993). While following this same trend for random rough surfaces, the *S*-band CPR can be significantly increased due to double-bounce scattering between smooth-sided rocks on the scale of a few decimeters (Campbell 2012; Neish et al. 2017). Generally consistent with this, Campbell et al. (1999) showed that the linear polarization ratio for highly reflective areas of Maxwell Montes peaks at ~0.5, while the CPR can reach values of around 1.2. The combination of the Arecibo and EnVision polarimetric data will thus more fully characterize the surface roughness on spatial scales up to a few radar wavelengths.

6. Conclusions

Arecibo radar maps of Venus remain important as we enter the era of renewed Venus exploration with VERITAS, DAVINCI, and EnVision. The dual-circular polarimetric data provide information on surface physical properties to complement orbital radar and infrared searches for ongoing volcanism and felsic material formed during a possible water-rich period. The long temporal span of the Earth-based observations allows for more accurate length-of-day estimates and the possibility of detecting large-scale surface changes. Mapping the surface of Venus represents a triumph of the early Arecibo radar program,

ORCID iDs

Bruce A. Campbell ● https://orcid.org/0000-0002-0428-8692

References

Campbell, B. A. 1995, USGS Open File Report, 95-519
Campbell, B. A. 2009, ITGRS, 47, 3480
Campbell, B. A. 2012, JGRE, 117, E06008
Campbell, B. A. 2016, Earth-Based Radar Observations of Venus, ARCB/NRAO-V-RTLS/GBT-3-DELAYDOPPLER-V1.0, NASA Planetary Data System
Campbell, B. A., Arvidson, R. E., & Shepard, M. K. 1993, JGR, 98, 17099
Campbell, B. A., & Campbell, D. B. 1992, JGR, 97, 16293
Campbell, B. A., Campbell, D. B., Carter, L. M., et al. 2019, Icar, 332, 19
Campbell, B. A., Campbell, D. B., & DeVries, C. 1999, JGRE, 104, 1897
Campbell, B. A., Campbell, D. B., Margot, J. L., et al. 2007, ITGRS, 45, 4032
Campbell, B. A., Morgan, G. A., Whitten, J. L., et al. 2017, JGRE, 122, 1580
Campbell, D. B., Head, J. W., Senske, D. A., et al. 1989, Sci, 246, 373
Carter, L. M., Campbell, D. B., & Campbell, B. A. 2004, JGRE, 109, E06009
Carter, L. M., Campbell, D. B., & Campbell, B. A. 2006, JGRE, 111, E06005
Carter, L. M., Campbell, D. B., & Campbell, B. A. 2011, IEEEP, 99, 770
Evans, J. V. 1968, in Radar Astronomy, ed. T. Hagfors & J. V. Evans (New York: McGraw-Hill)
Garvin, J. B., Arney, G., Getty, S., et al. 2020, LPSC, 51, 2599
Hagfors, T. 1967, RaSc, 2, 445
Harmon, J. K. 2002, ITGRS, 40, 1904
Hensley, S., Campbell, B., Perkovic-Martin, D., et al. 2020, in EEE Radar Conf. (RadarConf20) (Piscataway, NJ: IEEE), 1, doi:10.1109/RadarConf2043947.2020.9266323
Miller, F. 1981, ESA SAR Image Quality (N82-21458), 33
Muhleman, D. O. 1964, AJ, 69, 34
Neish, C. D., Hamilton, C. W., Hughes, S. S., et al. 2017, Icar, 281, 73
Pettengill, G. H., Ford, P. G., & Chapman, B. D. 1988, JGR, 93, 14881
Saunders, R. S., Spear, A. J., Allin, P. C., et al. 1992, JGR, 97, 13067
Smrekar, S. E., Hensley, S., Dyar, M. D., et al. 2021, LPSC, 52, 2211